Cell Reports
Physical Science

Article

Oxidation-driven synthetic molecular networks enable dynamic assembly and fluorescence modulation in living cells

Graphical abstract

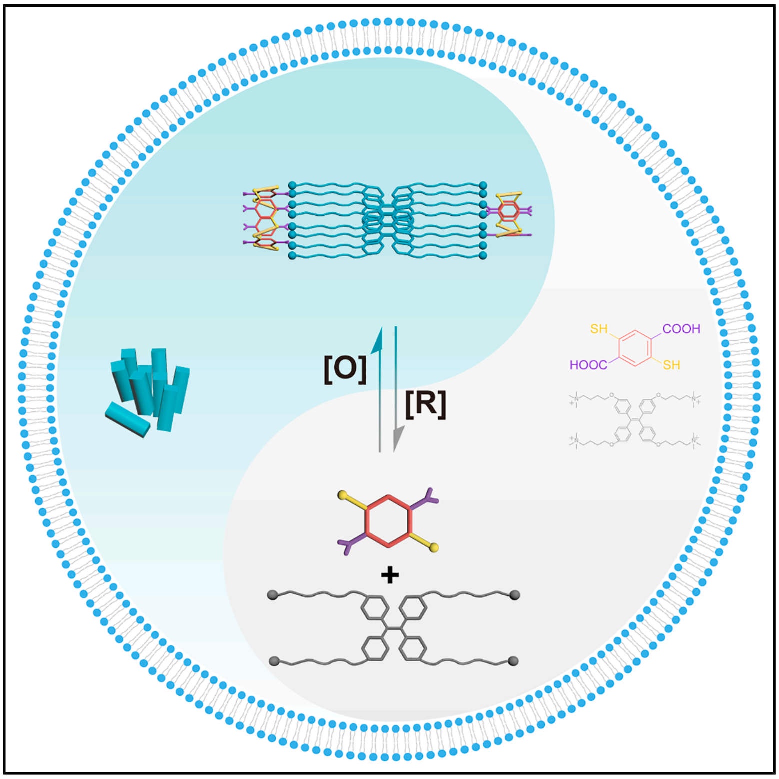

Highlights

- Oxidation-driven reversible macrocyclization and fluorescence activation
- Synthetic molecular networks assemble dynamically inside living cells
- System enables real-time monitoring of intracellular redox states

Authors

Jinghui Yang, Xin Wang, Xiaoxia Wu,
Yonglei Lyu,
Anastassios C. Papageorgiou,
Ermei Mäkilä, Jianwei Li

Correspondence

lijianwei@must.edu.mo

In brief

Yang et al. present an oxidation-driven synthetic molecular network that undergoes reversible macrocyclization and co-assembly with an aggregation-induced emission luminogen to autonomously assemble inside living cells. The system adaptively responds to intracellular redox fluctuations, enabling dynamic fluorescence modulation and real-time monitoring of cellular redox states.

Yang et al., 2025, Cell Reports Physical Science 6, 102922
November 19, 2025
https://doi.org/10.1016/j.xcrp.2025.102922

CellPress

Cell Reports
Physical Science

CellPress
OPEN ACCESS

Article

Oxidation-driven synthetic molecular networks enable dynamic assembly and fluorescence modulation in living cells

Jinghui Yang,[1,2,3] Xin Wang,[1,2,3] Xiaoxia Wu,[3] Yonglei Lyu,[1,2,3] Anastassios C. Papageorgiou,[4] Ermei Mäkilä,[5] and Jianwei Li[1,6,*]

[1]Macao Institute of Materials Science and Engineering (MIMSE), Faculty of Innovation Engineering, Macau University of Science and Technology, Taipa, Macao 999078, China
[2]Department of Chemistry, University of Turku, 20500 Turku, Finland
[3]MediCity Research Laboratory, University of Turku, 20520 Turku, Finland
[4]Turku Bioscience Centre, University of Turku, Åbo Akademi University, 20520 Turku, Finland
[5]Laboratory of Industrial Physics, Department of Physics and Astronomy, Institute of Dentistry, University of Turku, 20014 Turku, Finland
[6]Lead contact
*Correspondence: lijianwei@must.edu.mo
https://doi.org/10.1016/j.xcrp.2025.102922

SUMMARY

Systems chemistry explores emergent properties from interacting molecular networks, although extending these systems into biologically relevant environments remains challenging. Here, we report a synthetic molecular network that functions dynamically inside living cells by responding autonomously to oxidative stimuli. The network is built from dithiol precursors that undergo oxidation-driven macrocyclization and co-assemble with an aggregation-induced emission luminogen to form fluorescent nanostructures selectively under oxidative conditions. This process is reversible, allowing repeated cycles of fluorescence modulation. By exploiting intracellular oxidation as a stimulus, the system links systems chemistry with biological complexity and enables real-time monitoring of cellular redox dynamics through fluorescence. The fluctuations in signal directly reflect oxidative levels in living cells, providing a tool for tracking redox states. Our work demonstrates adaptive molecular self-assembly in a biological context and opens opportunities for redox bioimaging, diagnostics, and therapeutics regulated by cellular oxidative environments.

INTRODUCTION

Systems chemistry investigates networks of interacting molecules capable of exhibiting emergent properties such as adaptability, responsiveness, and dynamic self-organization.[1–3] Such chemical networks are fundamentally distinct from classical single-molecule studies, as their properties arise not merely from individual components but from their collective interactions and interdependencies.[4] While substantial progress has been made in understanding and designing synthetic molecular networks in controlled laboratory environments,[5,6] extending these principles into complex biological contexts—particularly within living cells—remains largely uncharted territory.

Intracellular environments provide an inherently dynamic and heterogeneous milieu characterized by crowdedness, spatial compartmentalization, and continuous biochemical fluctuations.[7,8] Oxidative processes within cells exemplify such complexity, playing critical roles in metabolic regulation,[9] cellular differentiation,[10] programmed cell death,[11] and response to oxidative stress. Imbalances in these redox networks are implicated in various pathological states, including cancer,[12,13] neurodegeneration,[14] and chronic inflammation.[15] However, current analytical techniques such as electrochemical sensing and mass spectrometry are predominantly invasive, requiring cell lysis or endpoint analyses,[16,17] and thus fail to capture the dynamic interplay of molecular networks at subcellular scales in real time.

In this context, fluorescence imaging provides a compelling approach due to its sensitivity, spatial resolution, and minimal invasiveness.[8] Conventional fluorescence-based tools predominantly consist of small-molecule probes or pre-synthesized nanomaterials. Despite their utility, small molecules frequently suffer from photobleaching and environmental instability, whereas nanomaterials often require elaborate pre-functionalization and exhibit limited cellular compatibility.[18,19] Thus, these approaches fail to leverage the dynamic network behaviors intrinsic to systems chemistry.

Recent advances have demonstrated that synthetic molecular systems can undergo dynamic reconfiguration driven by enzymatic or ionic stimuli[20] and even achieve supramolecular assembly inside living cells,[21] thereby establishing the feasibility and functional promise of operating chemical networks within biological environments. Disulfide-based dynamic self-assembly, including redox-controlled macrocyclization and network formation, has emerged as an important strategy.[22–24] Here, we introduce a systems chemistry approach designed explicitly

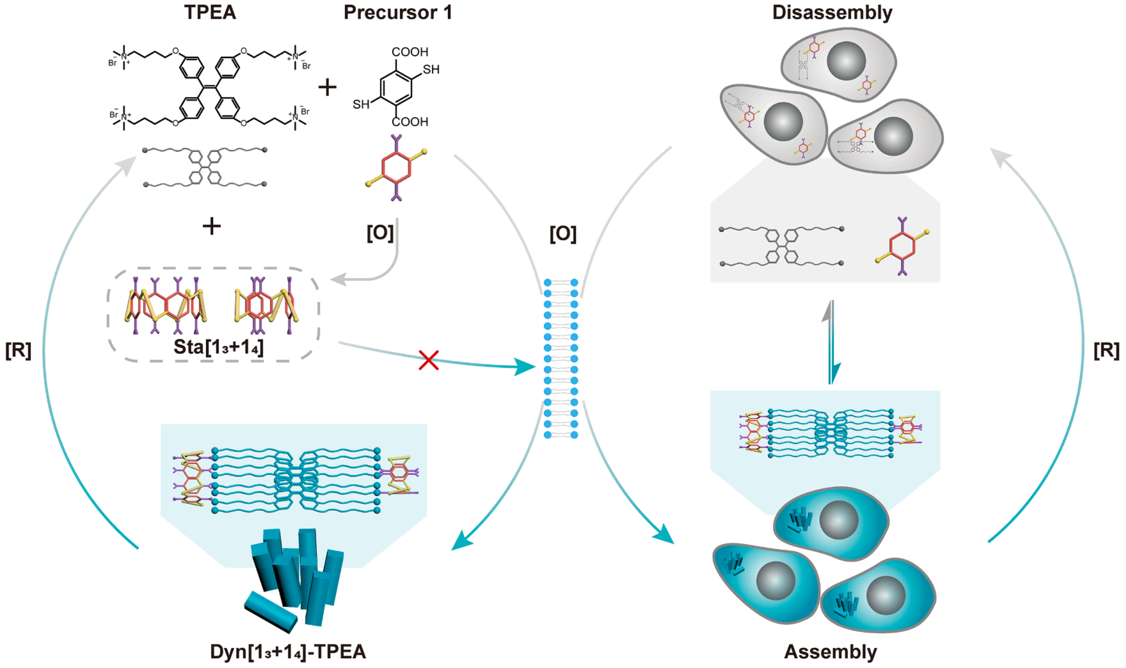

Scheme 1. Intracellular oxidation-driven assembly of fluorescent nanostructures

(Left) Upon intracellular or *in vitro* oxidation, dithiol-containing precursor **1** spontaneously macrocyclizes into dynamic disulfide-linked networks (**Dyn[1_3+1_4]**). In the presence of the AIE luminogen **TPEA**, these macrocyclic assemblies co-assemble into fluorescent nanostructures via synergistic electrostatic and host-guest interactions. (Right) In living cells, precursor **1** and **TPEA** are internalized and trafficked into lysosomes, where oxidative stimuli trigger progressive macrocyclization and co-assembly, leading to stepwise fluorescence activation. This dynamic process enables real-time visualization of intracellular redox states through reversible and adaptive molecular self-assembly.

to explore dynamic synthetic molecular networks within the intracellular environment. Our strategy employs a redox-responsive chemical network capable of undergoing spontaneous, stimulus-driven transformation directly inside living cells. Specifically, we developed molecular precursor **1** containing dithiol functionalities,[25–28] which upon intracellular oxidation spontaneously macrocyclize into dynamic disulfide-linked networks. These macrocyclic assemblies subsequently co-assemble with an aggregation-induced emission (AIE) luminogen,[29–34] specifically a tetraphenylethylene-derived quaternary ammonium salt (**TPEA**),[35] forming fluorescent nanostructures exclusively in response to oxidative conditions encountered within cells.

A distinctive feature of our approach lies in shifting the network assembly from controlled laboratory conditions into the complex biological context, allowing the chemical network to autonomously and adaptively respond to intracellular redox stimuli. Importantly, this oxidation-driven, intracellular self-assembly is reversible, as the formed disulfide networks can be readily reduced back to their original thiol-based precursors, thereby enabling dynamic and repeated fluorescence modulation. Such reversibility further emphasizes adaptability and responsiveness intrinsic to synthetic molecular networks within cellular environments. By successfully demonstrating dynamic intracellular assembly driven by oxidation-triggered molecular transformations, this work broadens the scope of systems chemistry, bridging synthetic chemical networks and living biological systems. This approach provides a framework for investigating emergent molecular behaviors directly within cells, providing fundamental insights into the design and functionality of adaptive chemical networks in biologically relevant contexts. This concept is schematically illustrated in Scheme 1.

RESULTS AND DISCUSSION

Oxidation-driven macrocycle formation and fluorescence activation

To explore the aggregation behavior of the AIE luminogen **TPEA** in the presence of molecular precursor **1**, we began by analyzing its fluorescence properties in PBS buffer (Figure S1). The critical aggregation concentration (CAC) of **TPEA** was determined to be 1.26×10^{-4} M. Below this threshold, no significant fluorescence was observed, indicating that free **TPEA** molecules did not aggregate sufficiently to restrict intramolecular phenyl ring rotations, which is a prerequisite for AIE activation. The complex chemical system was then prepared by mixing **TPEA** (0.5 mM) with molecular precursor **1** (1.0 mM) in PBS buffer. Upon oxidation over 72 h, the fluorescence intensity of **TPEA** increased significantly (Figure 1A), suggesting the formation of supramolecular assemblies that restricted intramolecular motions. To elucidate the chemical composition of the fluorescent assemblies, matrix-assisted laser desorption/ionization time-of-flight (MALDI-TOF) mass spectrometry analysis identified species trimer and tetramer (designated as **Dyn**[$\mathbf{1_3}$+$\mathbf{1_4}$]) as predominant, both in the presence and absence of **TPEA** (Figure S2). The

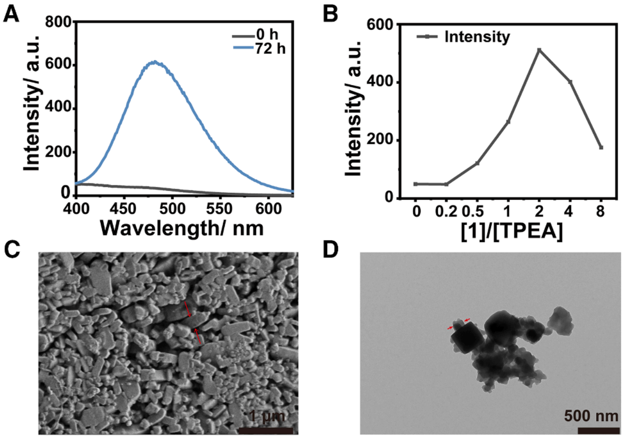

Figure 1. Oxidation-induced fluorescence activation and supramolecular aggregation of TPEA mediated by molecular precursor 1

(A) Fluorescence spectra of **TPEA** (0.5 mM) in the presence of precursor **1** (1.0 mM) before (0 h) and after (72 h) oxidation, showing significant emission enhancement upon oxidation-driven co-assembly in 50 mM PBS buffer (pH 7.4). Fluorescence spectra were recorded after dilution to 50 μM **TPEA**.

(B) Fluorescence intensity at 480 nm of **TPEA** at varying [**1**]/[**TPEA**] molar ratios after 72 h, with a maximum observed near the charge-balanced ratio (2:1), corresponding to optimal co-assembly in 50 mM PBS buffer (pH 7.4). The concentration of **TPEA** is 0.5 mM.

(C) SEM image of **Dyn[$\mathbf{1_3}$+$\mathbf{1_4}$]-TPEA** aggregates, exhibiting prism-like nanostructures. Scale bar, 1 μm. Sample prepared in aqueous solution at pH 7.4.

(D) TEM image of **Dyn[$\mathbf{1_3}$+$\mathbf{1_4}$]-TPEA**, showing densely packed nanostructures formed upon oxidation in 50 mM PBS buffer (pH 7.4). Scale bar, 500 nm.

measured trimer-to-tetramer ratios (1.30:1 without **TPEA**; 1.33:1 with **TPEA**) indicated that **TPEA** had no discernible effect on the product distribution. Since the oxidized products of precursor **1** exhibit no detectable peaks by high-performance liquid chromatography (HPLC) under the current conditions (Figure S3), which is likely attributable to both their aggregation into nanoscopic assemblies and the conformational diversity of the resulting macrocycles,[26,36] diffusion-ordered spectroscopy (DOSY) nuclear magnetic resonance (NMR) was employed to characterize the macrocycle distribution. The measurements revealed diffusion coefficients corresponding to the trimer (2.45×10^{-10} m^2/s) and tetramer (1.82×10^{-10} m^2/s) with an approximate ratio of 1:3 (25.47% vs. 74.53%, Figure S4). These findings demonstrate that the presence of **TPEA** does not exert a discernible effect on the distribution of oxidation products, while oxidative macrocyclization proceeds efficiently.

To better understand the mechanism underlying the pronounced fluorescence activation of **TPEA** upon oxidative assembly, a series of systems was prepared by varying the concentration of molecular precursor **1** while maintaining **TPEA** at a constant concentration. After 72 h of oxidation, **TPEA** fluorescence exhibited a sharp increase, reaching a maximum at molar ratios close to charge compensation (2:1) relative to **Dyn[$\mathbf{1_3}$+$\mathbf{1_4}$]** (Figure 1B). In contrast, **TPEA** alone showed negligible fluorescence change over the same time period, despite being used at a concentration above its critical aggregation concentration. Furthermore, immediate fluorescence enhancement was observed when **Dyn[$\mathbf{1_3}$+$\mathbf{1_4}$]** was directly added to a **TPEA** solution, as shown in Figure S5 and Video S1 (a time-lapse recording showing fluorescence activation of **Dyn[$\mathbf{1_3}$+$\mathbf{1_4}$]** and **TPEA**), providing additional evidence that the fluorescence activation is specifically induced by the interaction between **TPEA** and **Dyn[$\mathbf{1_3}$+$\mathbf{1_4}$]**. At this optimal ratio, dynamic light scattering (DLS) measurements revealed the formation of nanoparticles with an average hydrodynamic diameter of approximately 560 nm (Figure S6). Scanning electron microscopy (SEM) further confirmed the development of well-defined tetragonal prism structures with heights ranging from 500 to 600 nm (Figure 1C), while transmission electron microscopy (TEM) confirmed square cross-sections of approximately 150 nm (Figure 1D). As a control, precursor **1** was oxidized in the absence of **TPEA**, which showed neither fluorescence nor Tyndall effect, confirming that oxidative assembly requires the presence of both components (Figure S7). Despite their well-defined prism-like morphology, powder X-ray diffraction (PXRD) analysis of the assemblies revealed no detectable diffraction peaks, indicating a lack of long-range crystallinity and supporting the non-crystalline nature of the supramolecular network. Beyond the optimal charge balance, a progressive decrease in fluorescence intensity was observed, suggesting partial disassembly of the supramolecular network. In systems prepared with higher initial concentrations of precursor **1**, oxidation produced an excess of **Dyn[$\mathbf{1_3}$+$\mathbf{1_4}$]**, which destabilized the electrostatic and host-guest interactions critical for network integrity. DLS analysis revealed the emergence of a new particle population centered at approximately 80 nm, while zeta-potential measurements showed a decrease in surface potential to −48.5 mV. These findings indicate that while controlled oxidative assembly enables the formation of ordered, fluorescent supramolecular structures, excess oxidation products disrupt the delicate dynamic balance, leading to disassembly into smaller, less organized complexes.

Supramolecular interactions promote oxidation-induced network formation

To monitor the dynamic evolution of the oxidation-induced assembly, a system comprising molecular precursor **1** (1.0 mM) and **TPEA** (0.5 mM) was prepared in PBS buffer (pH 7.4). At the initial stage, negligible fluorescence was detected, indicating that **TPEA** molecules remained freely dispersed. As oxidation progressed, a sharp 10-fold increase in fluorescence intensity was observed after 12 h of incubation (Figure 2A). HPLC analysis revealed that precursor **1** was rapidly consumed during this period and was nearly completely oxidized after 12 h of oxidation. This consumption profile closely resembled that of precursor **1** alone (Figure S8), indicating that the presence of **TPEA** does not markedly affect the oxidation of precursor **1**. Notably, no distinct oxidation product peaks were detected, likely due to the stabilization of oxidized species within nanoparticle assemblies, rendering them insoluble and inaccessible to chromatographic separation. Consistent with these observations, fluorescence spectra showed that fluorescence saturation coincided with the complete oxidation of precursor **1** (Figure 2A). Simultaneously, optical density (OD) measurements revealed a gradual increase during the oxidation process, stabilizing after 12 h (Figure 2B), further confirming the formation and stabilization of oxidation-induced supramolecular aggregates. Together,

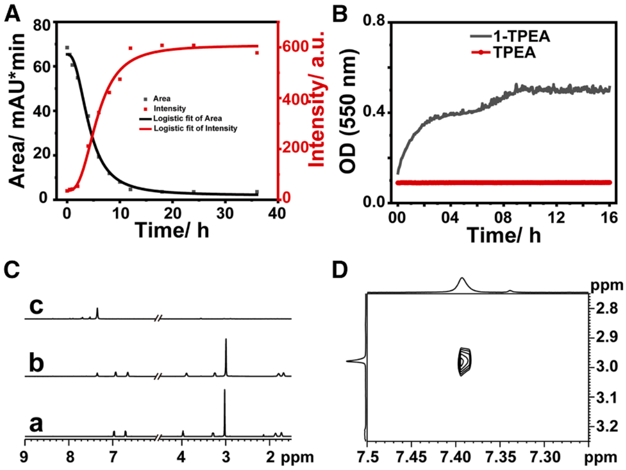

Figure 2. Time-dependent oxidation and supramolecular interaction drive fluorescence activation in the precursor 1-TPEA system

(A) Simultaneous monitoring of molecular precursor **1** (1.0 mM) consumption (HPLC peak area, black) and **TPEA** (0.5 mM) fluorescence intensity at 480 nm (red) over time in 50 mM PBS buffer (pH 7.4). Fluorescence spectra were recorded after dilution to 50 μM **TPEA**. Logistic fitting reveals synchronous oxidation and fluorescence enhancement reaching saturation after approximately 12 h.

(B) Optical density (OD) changes of **1-TPEA** (1.0 mM/0.5 mM) in 50 mM PBS buffer (pH 7.4) mixture over time, indicating nanoparticle formation driven by oxidation. No significant OD change is observed for **TPEA** alone.

(C) Partial ^{1}H NMR spectra (600 MHz) of (a) **TPEA** (0.5 mM), (b) **TPEA** (0.5 mM) mixed with precursor **1** (1.0 mM), and (c) precursor **1** (1.0 mM) alone, showing chemical-shift changes indicative of electrostatic interactions. The spectra were recorded at 298 K in 50 mM phosphate buffer (pD 7.4, D_2O).

(D) 2D NOESY spectrum (600 MHz) of the **1-TPEA** mixture (1.0 mM/0.5 mM), confirming intermolecular proximity between precursor **1** and the trimethylammonium groups of **TPEA**. The spectra were recorded at 298 K in 50 mM phosphate buffer (pD 7.4, D_2O).

these results demonstrate that oxidative conversion of precursor **1** triggers a dynamic aggregation process that restricts intramolecular motions of **TPEA**, thereby activating fluorescence through network assembly.

Since NMR signals disappeared after complete oxidation due to nanoparticle formation, we focused on the initial stages of the oxidation process to investigate the molecular events leading to dynamic network assembly. HPLC and DOSY NMR experiments identified a peak at 7.37 ppm corresponding to precursor **1**, with a diffusion coefficient of 7.35 × 10^{-10} m^2/s (Figure S9). Further insights into the early-stage interactions were obtained via ^{1}H NMR spectroscopy (Figure 2C). Upon addition of **TPEA**, the signal of precursor **1** shifted downfield, while all proton signals associated with **TPEA** shifted upfield, consistent with electrostatic and host-guest interactions that precede oxidation-driven assembly. Two-dimensional nuclear Overhauser effect spectroscopy (NOESY) experiments revealed NOE correlations between the aromatic proton of precursor **1** and the trimethylammonium group (Hg) of **TPEA** (Figure 2D), confirming spatial proximity during the early oxidation stage. Concurrently, the T_2 relaxation times of both precursor **1** and **TPEA** decreased significantly, particularly in the low-field region of **TPEA** (Table S1).[37,38] These results suggest that electrostatic complexation restricts intramolecular motions of **TPEA** at an early stage, pre-organizing the system for subsequent oxidative network formation. Comparison with the oxidation behavior of precursor **1** alone revealed that in the presence of **TPEA**, oxidation proceeded with exclusive consumption of the precursor without detectable formation of discrete oxidized species or free macrocycles (Figure S10). This behavior highlights that strong electrostatic and host-guest interactions actively direct the oxidative assembly pathway, stabilizing dynamic aggregates and preventing uncontrolled network expansion. To validate the generality of this interaction mechanism, a phenol-derived quaternary ammonium salt (**PQAS**) was employed as a model for **TPEA**.[35] Upon complexation, **PQAS** exhibited uniform upfield shifts in proton signals and pronounced reductions in T_2 relaxation times, particularly in the aromatic region (Figure S11). These results collectively demonstrate that early electrostatic and host-guest interactions between **TPEA** and precursor **1** pre-organize the system at the onset of oxidation, while progressive oxidative assembly further restricts the intramolecular motions of **TPEA**. This dynamic reorganization ultimately leads to the formation of **Dyn[1_3+1_4]-TPEA** assemblies, stabilizing fluorescent supramolecular networks through oxidation-driven aggregation.

Gradual oxidation enables functional network assembly

Based on these experimental findings, we propose that the oxidation of precursor **1** triggers the aggregation of **TPEA** through electrostatic and host-guest interactions, leading to fluorescence activation. To further assess the importance of the oxidation-driven dynamic assembly process, we compared the *in situ* oxidation system with a control prepared from **TPEA** and pre-oxidized trimer **1_3** and tetramer **1_4** (collectively referred to as **Sta[1_3+1_4]**). The **Sta[1_3+1_4]-TPEA** sample exhibited initial fluorescence; however, within 30 min, a marked decrease in fluorescence intensity and a concomitant increase in OD were observed, indicating uncontrolled aggregation and precipitation, which rendered further analysis infeasible (Figure S12). In contrast, *in situ* oxidation of precursor **1** in the presence of **TPEA** produced stable fluorescence and well-dispersed nanostructures, highlighting that gradual oxidative assembly enables controlled nanoparticle formation while preventing excessive aggregation. To further verify the necessity of thiol-driven oxidative assembly, terephthalic acid (**TA**), a dicarboxylic molecule lacking thiol groups, was introduced as a control. The **TA**-based system failed to induce fluorescence enhancement (Figure S13), confirming the essential role of thiol functionalities in initiating the oxidation-induced aggregation process. Together, these results demonstrate that gradual oxidation, rather than pre-oxidation, is critical for directing the formation of stable and functional supramolecular nanostructures, aligning with the design principles of dynamic systems chemistry.

Redox-responsive reconfiguration of the supramolecular network

The redox responsiveness of the **Dyn[1_3+1_4]-TPEA** system was systematically evaluated by exploiting the reducibility of disulfide bonds to thiols using dithiothreitol (DTT). Controlled disassembly experiments were performed under varying DTT concentrations to monitor the corresponding fluorescence responses. Upon

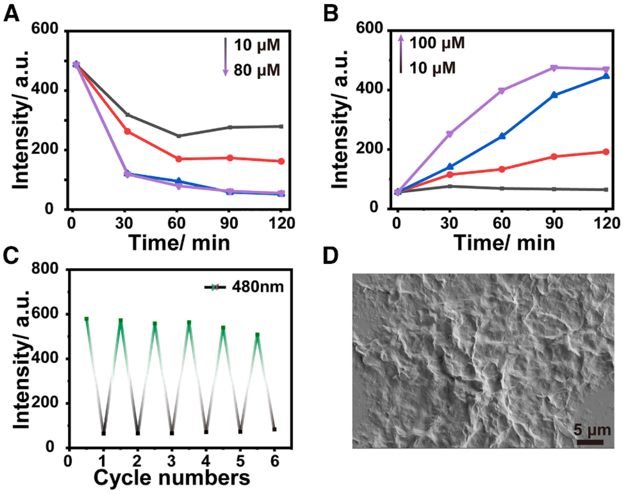

Figure 3. Redox responsiveness and recyclability of the Dyn[1_3+1_4]-TPEA assembly system

(A) Fluorescence intensity at 480 nm changes over time after addition of different concentrations (10–80 μM) of DTT in 50 mM PBS buffer (pH 7.4), showing concentration-dependent fluorescence quenching due to disulfide bond reduction. Fluorescence spectra were recorded after dilution to 50 μM **TPEA**.

(B) After reduction by 40 μM DTT for 2 h, subsequent reoxidation by H_2O_2 (10–100 μM) in PBS buffer (pH 7.4) restores fluorescence in a dose- and time-dependent manner.

(C) Fluorescence intensity at 480 nm over six redox cycles (DTT/H_2O_2), demonstrating excellent reversibility and system stability.

(D) SEM image of **Dyn[1_3+1_4]-TPEA** assemblies in aqueous medium (pH 7.4) after DTT treatment, showing that the original nanostructures are disrupted and disassembled upon reduction. Scale bar, 5 μm.

DTT addition, fluorescence intensity exhibited a consistent decline. At lower DTT concentrations (10 μM and 20 μM), fluorescence stabilized after approximately 60 min, indicating the establishment of a redox equilibrium. In contrast, at a higher DTT concentration (40 μM), fluorescence intensity was significantly quenched within 120 min, reflecting more extensive disulfide bond reduction (Figure 3A). Concurrently, SEM revealed a complete disappearance of the quadrangular prism morphology of the **Dyn[1_3+1_4]-TPEA** assemblies upon reduction, further confirming aggregate disassembly induced by disulfide cleavage (Figure 3D). Given the slow reoxidation rate mediated by atmospheric oxygen, hydrogen peroxide (H_2O_2) was introduced to accelerate the reassembly process. Remarkably, fluorescence intensity was nearly fully restored within 2 h at an H_2O_2 concentration of 50 μM (Figure 3B). To further assess the durability and reversibility of the system, a recyclable redox cycling experiment was conducted,[39] involving sequential reduction with DTT and reoxidation with H_2O_2. Over six cycles, fluorescence intensity displayed only minor variations, demonstrating the excellent robustness and stability of the oxidation-induced dynamic network (Figure 3C).

Stimulus-responsive network assembly enables intracellular redox imaging

Before assessing the **Dyn[1_3+1_4]-TPEA** system in cellular environments, the cytotoxicity of the molecular precursor **1**, **TPEA**, and **Sta[1_3+1_4]** were evaluated using MTT assays. MCF-7S breast cancer cells were treated with varying concentrations of molecular precursor **1**, **TPEA**, and **Sta[1_3+1_4]**. As shown in Figures 4A and S14, the IC_{50} of the molecular precursor **1**, **TPEA**, and **Sta[1_3+1_4]** are 2.06 mM, 1.05 mM, and 2.42 mM, respectively, indicating low inherent cytotoxicity for all components. Given that pre-formed **Dyn[1_3+1_4]-TPEA** assemblies formed large aggregates unsuitable for direct cellular uptake (Figures S15 and S16), a stepwise assembly strategy was adopted. In this approach, **TPEA** and precursor **1** were sequentially introduced into cells, enabling intracellular aggregation under biologically relevant oxidative conditions (Scheme 2). Importantly, we confirmed that precursor **1** remains oxidizable even in the presence of 5.0 mM glutathione (Figure S17), supporting its compatibility with intracellular redox environments. Based on cytotoxicity evaluations, a **TPEA** concentration of 0.2 mM was selected for subsequent studies. At this lower concentration, a pronounced fluorescence enhancement was observed both in PBS buffer and in complete cell-culture medium,

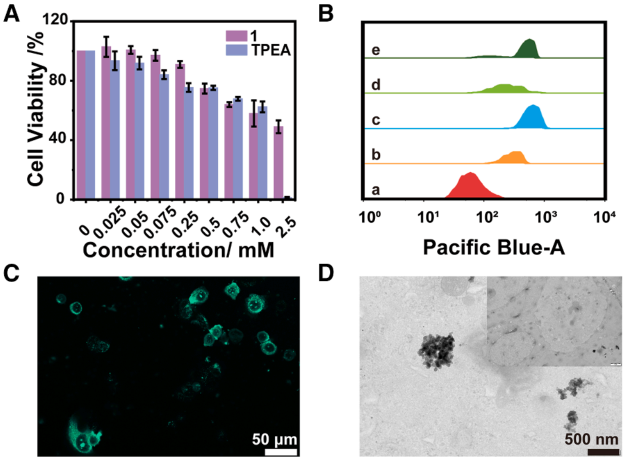

Figure 4. Cytocompatibility and intracellular assembly of precursor 1-TPEA fluorescent nanostructures

(A) Cell viability of MCF-7S cells treated with increasing concentrations of precursor **1** and **TPEA**, measured by MTT assay, showing low cytotoxicity for both components. Data are presented as mean ± SD from three independent experiments (*n* = 3). Cells were incubated for 24 h under standard culture conditions (37°C, 5% CO_2, complete culture medium).

(B) Flow-cytometry analysis of Pacific Blue-A fluorescence in MCF-7S cells under different conditions: (a) untreated; (b) **TPEA** only (0.2 mM, 30 min incubation); (c) **Dyn[1_3+1_4]-TPEA**, prepared by sequential incubation with **TPEA** (0.2 mM, 30 min) followed by precursor **1** (0.4 mM, 12 h); (d) same as (c) with additional DTT treatment (50 μM, 120 min); and (e) same as (d) with subsequent H_2O_2 treatment (50 μM, 120 min). All incubations were conducted at 37°C in complete culture medium (5% CO_2), with PBS washes between each step. Fluorescence enhancement upon oxidation and reversible modulation by redox stimuli confirm the redox responsiveness of the intracellular assemblies.

(C) Confocal fluorescence image of MCF-7S cells after sequential incubation with **TPEA** (0.2 mM, 30 min) followed by precursor **1** (0.4 mM, 12 h) in complete culture medium. Cells were washed with PBS before imaging, showing punctate lysosomal fluorescence. Scale bar, 50 μm.

(D) Bio-TEM image of MCF-7S cells treated by the same sequential incubation protocol (**TPEA** 0.2 mM, 30 min; precursor **1**, 0.4 mM, 12 h) in complete culture medium, revealing electron-dense nanoparticles localized within lysosomal compartments. Scale bar, 500 nm.

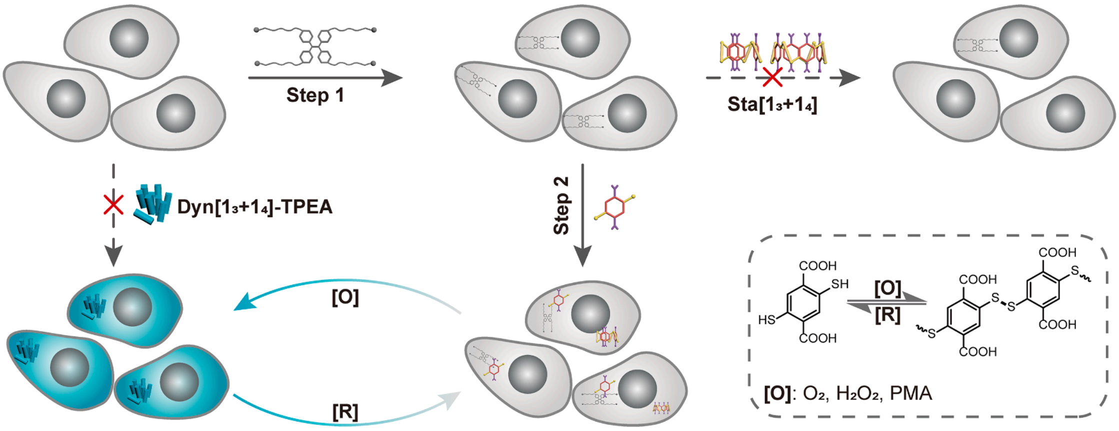

Scheme 2. Stepwise cellular incubation strategy for the *in situ* construction and redox control of fluorescent assemblies

MCF-7S cells were first incubated with the AIE luminogen **TPEA** (0.2 mM, 30 min) in complete culture medium to facilitate membrane integration (step 1), followed by treatment with molecular precursor **1** (0.4 mM, 12 h) in complete culture medium (step 2). Precursor **1** readily entered cells and underwent intracellular oxidation, triggering the *in situ* formation of fluorescent **Dyn[1_3+1_4]-TPEA** assemblies, similar to other *in situ* dynamic covalent transformations in living cells. In contrast, the static macrocycle **Sta[1_3+1_4]** failed to generate intracellular fluorescence under confocal imaging, suggesting limited cellular uptake or insufficient assembly capability. Preformed **Dyn[1_3+1_4]-TPEA** particles exhibited strong aggregation behavior and led to significant cytotoxicity under imaging conditions. These observations underscore the importance of *in situ* activation for achieving functional intracellular assembly. The resulting structures responded reversibly to oxidative (O_2, H_2O_2, and PMA) and reductive (DTT and glutathione [GSH]) stimuli.

confirming effective aggregation under physiological conditions (Figure S18).

To experimentally validate intracellular dynamic assembly under these conditions, **TPEA** was first incubated with MCF-7S cells for 0.5 h, followed by the addition of precursor **1**. Confocal laser scanning microscopy (CLSM) revealed a significant enhancement of **TPEA** fluorescence after 12 h of incubation, confirming successful oxidation-induced aggregation within the cellular environment (Figure 4C).[40] In untreated cells, no fluorescence enhancement was observed. Similarly, when **Sta[1_3+1_4]** was introduced into cells, no intracellular fluorescence was detected, likely due to its highly charged structure that impedes membrane permeation. In contrast, precursor **1** underwent intracellular oxidation to form fluorescent assemblies, as confirmed by bio-TEM analysis showing electron-dense nanoparticles localized within lysosomes (Figure 4D). In control experiments, no nanoparticles were observed (Figure S19). Following confirmation of intracellular assembly, the redox responsiveness of the system was further explored using flow cytometry and CLSM. MCF-7S cells incubated with **TPEA** and the molecular precursor **1** exhibited increased Pacific Blue-A fluorescence compared to untreated cells or cells treated with **TPEA** alone, indicating successful intracellular assembly of **Dyn[1_3+1_4]-TPEA**. Treatment with DTT resulted in a significant decrease in fluorescence, reflecting disulfide bond reduction, while subsequent addition of H_2O_2 restored fluorescence, confirming the redox activity of the system within living cells (Figure 4B). Notably, 2-h incubation with either DTT or H_2O_2 showed negligible cytotoxicity, as evidenced by cell viability exceeding 95% (Figure S20).

Adaptive and reversible behavior of the synthetic network in living cells

To explore the dynamic behavior of **Dyn[1_3+1_4]-TPEA** within living cells, real-time CLSM with continuous imaging was employed.[41] Cells were first incubated with **TPEA** for 0.5 h, followed by treatment with molecular precursor **1**, enabling gradual intracellular fluorescence activation under physiological oxidative conditions (Scheme 2).[42] Time-lapse imaging was conducted every 5 min, capturing the progressive increase in fluorescence intensity. By plotting the relative fluorescence intensity over time, a distinct evolution profile was observed: fluorescence remained relatively stable during the first 6 h, followed by a significant increase around 8 h and reaching a plateau between 10 and 12 h (Figures 5A [top] and 5B). This delay is likely attributed to the endocytic uptake and intracellular processing of precursor **1**, postponing oxidation-induced aggregation. Notably, at the plateau phase, the fluorescence intensity reached approximately three times its initial value, confirming substantial oxidation-driven assembly within the cellular environment. Consistent with this delayed profile, the observed 6- to 8-h fluorescence activation likely arises from both the intrinsic oxidation kinetics of precursor **1** and its gradual trafficking into acidic intracellular compartments. This is supported by NH_4Cl treatment,[43,44] which elevates endolysosomal pH and effectively suppresses intracellular fluorescence activation, whereas oxidation and fluorescence activation proceed efficiently under *in vitro* conditions (Figure S21).

To dynamically monitor the redox behavior of **Dyn[1_3+1_4]-TPEA** at the cellular level, real-time CLSM with continuous imaging was employed, enabling non-invasive visualization of intracellular redox dynamics while avoiding cell disruption and organelle isolation (Scheme 2). Cells were pre-incubated with **TPEA**, followed by the addition of molecular precursor **1**, allowing fluorescence activation before sequential treatment with DTT and H_2O_2 to induce reduction and oxidation processes, respectively. Time-lapse imaging was performed every 2.5 min over a 240-min period, revealing distinct fluorescence dynamics. Upon DTT addition, a rapid "brightness-to-darkness" transition was observed, with

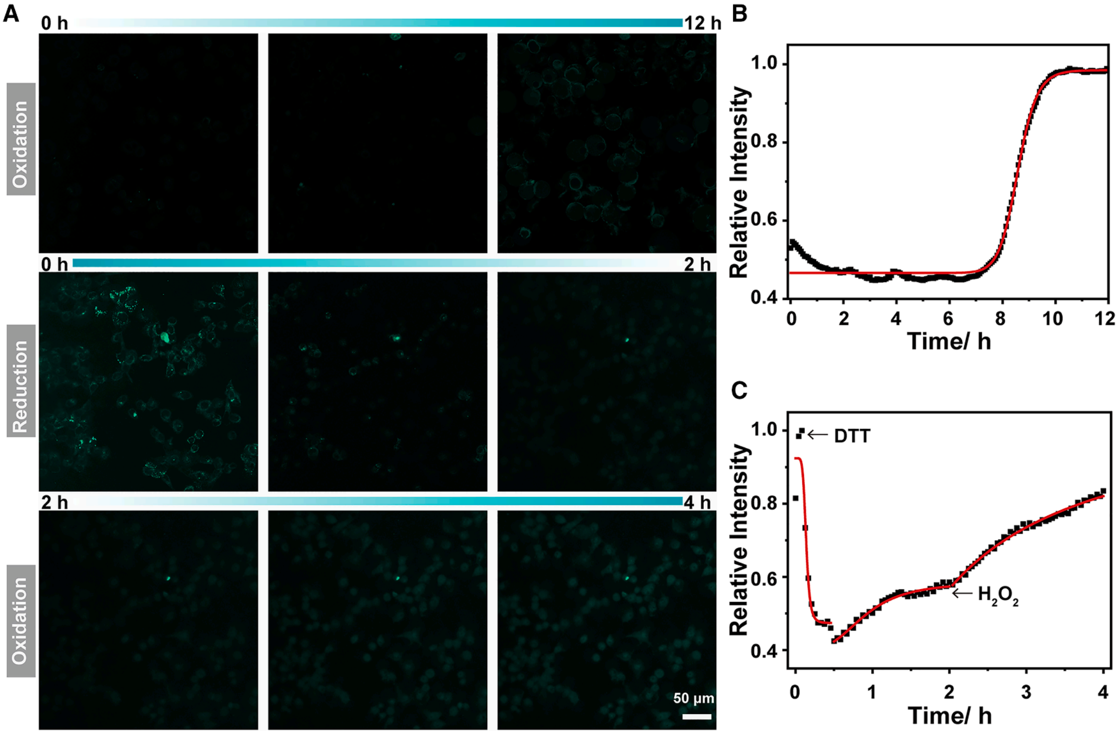

Figure 5. Real-time confocal imaging of intracellular redox dynamics using the precursor 1-TPEA system

(A) CLSM images of MCF-7S cells showing (top) time-dependent fluorescence activation during intracellular oxidation, with images taken at 0 h, 6 h, and 12 h after sequential incubation with **TPEA** (0.2 mM, 30 min) followed by precursor **1** (0.4 mM, 12 h) in complete culture medium; (middle) fluorescence quenching in cells subjected to the same initial treatment as in the top panel, followed by incubation with DTT (50 μM) in complete culture medium, with images recorded at 0 h, 1 h, and 2 h post treatment; and (bottom) fluorescence recovery upon subsequent treatment of the same cells with H_2O_2 (50 μM) in complete culture medium, with images taken at 2.1 h, 3 h, and 4 h relative to initial DTT treatment. Middle and bottom panels were acquired from the same batch of cells. Scale bar, 50 μm.

(B) Fluorescence intensity profile corresponding to the oxidation stage in (A [top]), showing progressive fluorescence enhancement associated with intracellular oxidation.

(C) Fluorescence intensity profile corresponding to the reduction and reoxidation stages in (A [middle and bottom]), demonstrating reversible fluorescence modulation in response to intracellular redox changes. Black dots represent experimental measurements; red lines correspond to fitted fluorescence intensity curves.

fluorescence intensity sharply decreasing during the initial 30 min due to the reduction of **Dyn[$\mathbf{1_3}$+$\mathbf{1_4}$]-TPEA** and the subsequent disruption of oxidation-induced aggregates. In the second phase (30–120 min), fluorescence gradually recovered, reaching a plateau around 1.5–2 h (Figures 5A [middle] and 5C), corresponding to spontaneous reoxidation within the intracellular environment and resembling the fluorescence evolution trend observed in Figure 5A (top). In the final phase (120–240 min), the introduction of exogenous H_2O_2 further promoted the oxidation of molecular precursor **1**, leading to accelerated fluorescence enhancement and the formation of additional oxidation-induced aggregates (Figures 5A [bottom] and 5C). These findings offer insight into the redox kinetics of molecular precursor **1** and its interaction with **TPEA**, demonstrating the dynamic and reversible nature of the system in living cells.[45]

As a comparison, we investigated the redox-responsive behavior of **Dyn[$\mathbf{1_3}$+$\mathbf{1_4}$]-TPEA** in human dermal fibroblasts (HDFs), which are known to exhibit lower intracellular reactive oxygen species (ROS) levels.[46] In contrast, MCF-7 cells possess relatively high basal ROS levels, with the predominant species being superoxide ($O_2^{\cdot -}$) and hydrogen peroxide (H_2O_2).[12] At the same concentrations used for MCF-7S cells, HDF cells maintained over 80% viability, indicating acceptable cytocompatibility under these conditions. However, real-time CLSM imaging revealed no appreciable fluorescence enhancement throughout the imaging period, suggesting that insufficient oxidative stress in HDF cells fails to trigger the intracellular assembly process (Figure S22). These results highlight the importance of the cellular redox environment in regulating the activation and dynamics of the **Dyn[$\mathbf{1_3}$+$\mathbf{1_4}$]-TPEA** system.

To further assess the responsiveness of the **Dyn[$\mathbf{1_3}$+$\mathbf{1_4}$]-TPEA** system to intracellular oxidative stimuli, ROS production was stimulated using phorbol 12-myristate 13-acetate (PMA). PMA treatment had a negligible effect on fluorescence in the cell-free solution but markedly enhanced fluorescence in living cells (Figure S23), indicating that the enhancement originates from intracellular ROS production. Cells pre-incubated with **TPEA** and precursor **1** initially exhibited fluorescence activation, which significantly decreased upon DTT treatment, likely reflecting disulfide bond reduction. Subsequent PMA stimulation (10–50 μM, 2 h) induced a substantial fluorescence recovery, confirming that the system could dynamically respond to intracellular ROS generation (Figure S24). These results further support the robust reversibility and adaptability of the **Dyn [1_3+1_4]-TPEA** network, enabling real-time visualization of redox processes under physiologically relevant conditions.

In conclusion, we have established an oxidation-driven synthetic molecular network capable of dynamic self-assembly within living cells, initiated by intracellular oxidative stimuli. Through the design of dithiol-based molecular building blocks that undergo oxidative macrocyclization and co-assemble with an aggregation-induced emission luminogen, we achieved a controlled transformation from small molecular units into adaptive supramolecular networks under biologically relevant conditions. The dynamic modulation of fluorescence provides a direct readout of the reversible assembly and disassembly of the molecular network, highlighting the system's responsiveness to intracellular redox fluctuations. By demonstrating stimulus-responsive assembly and reversible functional emergence within living cells, this work broadens the scope of systems chemistry into complex biological environments and offers a versatile framework for investigating adaptive molecular networks and emergent behaviors in living systems.

METHODS

Details of methods can be found in supplemental methods.

RESOURCE AVAILABILITY

Lead contact

Requests for further information and resources should be directed to and will be fulfilled by the lead contact, Dr. Jianwei Li (lijianwei@must.edu.mo).

Materials availability

This study did not generate new unique reagents.

Data and code availability

- The data supporting this study are available in the manuscript and supplemental information.
- This paper does not report any original code.
- Any additional information required to reanalyze the data reported in this paper is available from the lead contact upon request.

ACKNOWLEDGMENTS

We are grateful for financial support from the National Natural Science Foundation of China (22161016), the Macau University of Science and Technology, and the Sigrid Jusélius Foundation (Senior Researcher Fellowship). J.Y. and X.W. acknowledge support from the China Scholarship Council (CSC). We thank the Turku Center for Chemical and Molecular Analytics for providing NMR and mass spectrometry, and the Electron Microscopy Laboratory (Institute of Biomedicine, University of Turku) and Biocenter Finland for TEM imaging.

AUTHOR CONTRIBUTIONS

J.Y. conceived the idea, carried out the synthesis, characterization, and cell experiments, and wrote the manuscript; X. Wang and X. Wu assisted with cell experiments; Y.L. and X. Wang carried out part of the synthesis; A.C.P. carried out the PXRD characterization; E.M. performed the SEM characterization; and J.L. supervised the research and wrote the paper.

DECLARATION OF INTERESTS

The authors declare no competing interests.

SUPPLEMENTAL INFORMATION

Supplemental information can be found online at https://doi.org/10.1016/j.xcrp.2025.102922.

Received: May 15, 2025
Revised: August 24, 2025
Accepted: October 3, 2025
Published: November 3, 2025

REFERENCES

1. Mattia, E., and Otto, S. (2015). Supramolecular systems chemistry. Nat. Nanotechnol. *10*, 111–119. https://doi.org/10.1038/nnano.2014.337.
2. Ashkenasy, G., Hermans, T.M., Otto, S., and Taylor, A.F. (2017). Systems chemistry. Chem. Soc. Rev. *46*, 2543–2554. https://doi.org/10.1039/c7cs00117g.
3. Sheehan, F., Sementa, D., Jain, A., Kumar, M., Tayarani-Najjaran, M., Kroiss, D., and Ulijn, R.V. (2021). Peptide-Based Supramolecular Systems Chemistry. Chem. Rev. *121*, 13869–13914. https://doi.org/10.1021/acs.chemrev.1c00089.
4. Ghosh, S., Baltussen, M.G., Ivanov, N.M., Haije, R., Jakštaitė, M., Zhou, T., and Huck, W.T.S. (2024). Exploring emergent properties in enzymatic reaction networks: design and control of dynamic functional systems. Chem. Rev. *124*, 2553–2582. https://doi.org/10.1021/acs.chemrev.3c00681.
5. Santos-Moreno, J., Tasiudi, E., Stelling, J., and Schaerli, Y. (2020). Multistable and dynamic CRISPRi-based synthetic circuits. Nat. Commun. *11*, 2746. https://doi.org/10.1038/s41467-020-16574-1.
6. Semenov, S.N., Kraft, L.J., Ainla, A., Zhao, M., Baghbanzadeh, M., Campbell, V.E., Kang, K., Fox, J.M., and Whitesides, G.M. (2016). Autocatalytic, bistable, oscillatory networks of biologically relevant organic reactions. Nature *537*, 656–660. https://doi.org/10.1038/nature19776.
7. Chagri, S., Ng, D.Y.W., and Weil, T. (2022). Designing bioresponsive nanomaterials for intracellular self-assembly. Nat. Rev. Chem *6*, 320–338. https://doi.org/10.1038/s41570-022-00373-x.
8. Geng, Y., Wang, Z., Zhou, J., Zhu, M., Liu, J., and James, T.D. (2023). Recent progress in the development of fluorescent probes for imaging pathological oxidative stress. Chem. Soc. Rev. *52*, 3873–3926. https://doi.org/10.1039/D2CS00172A.
9. Schieber, M., and Chandel, N.S. (2014). ROS function in redox signaling and oxidative stress. Curr. Biol. *24*, R453–R462. https://doi.org/10.1016/j.cub.2014.03.034.
10. Bigarella, C.L., Liang, R., and Ghaffari, S. (2014). Stem cells and the impact of ROS signaling. Development *141*, 4206–4218. https://doi.org/10.1242/dev.107086.
11. Redza-Dutordoir, M., and Averill-Bates, D.A. (2016). Activation of apoptosis signalling pathways by reactive oxygen species. Bba-Mol Cell Res *1863*, 2977–2992. https://doi.org/10.1016/j.bbamcr.2016.09.012.
12. Liou, G.-Y., and Storz, P. (2010). Reactive oxygen species in cancer. Free Radic. Res. *44*, 479–496. https://doi.org/10.3109/10715761003667554.
13. Nakamura, H., and Takada, K. (2021). Reactive oxygen species in cancer: Current findings and future directions. Cancer Sci. *112*, 3945–3952. https://doi.org/10.1111/cas.15068.
14. Butterfield, D.A., and Halliwell, B. (2019). Oxidative stress, dysfunctional glucose metabolism and Alzheimer disease. Nat. Rev. Neurosci. *20*, 148–160. https://doi.org/10.1038/s41583-019-0132-6.
15. van der Vliet, A., and Janssen-Heininger, Y.M. (2014). Hydrogen peroxide as a damage signal in tissue injury and inflammation: murderer, mediator, or messenger? J. Cell. Biochem. *115*, 427–435. https://doi.org/10.1002/jcb.24683.
16. Wu, L., Sedgwick, A.C., Sun, X., Bull, S.D., He, X.-P., and James, T.D. (2019). Reaction-based fluorescent probes for the detection and imaging

of reactive oxygen, nitrogen, and sulfur species. Acc. Chem. Res. *52*, 2582–2597. https://doi.org/10.1021/acs.accounts.9b00302.

17. Zhao, Y., Jin, K.Q., Li, J.D., Sheng, K.K., Huang, W.H., and Liu, Y.L. (2025). Flexible and stretchable electrochemical sensors for biological monitoring. Adv. Mater. *37*, 2305917. https://doi.org/10.1002/adma.202305917.
18. Smith, A.M., Duan, H., Mohs, A.M., and Nie, S. (2008). Bioconjugated quantum dots for in vivo molecular and cellular imaging. Adv. Drug Deliv. Rev. *60*, 1226–1240. https://doi.org/10.1016/j.addr.2008.03.015.
19. Kaymaz, S.V., Nobar, H.M., Sarıgül, H., Soylukan, C., Akyüz, L., and Yüce, M. (2023). Nanomaterial surface modification toolkit: Principles, components, recipes, and applications. Adv. Colloid Interface Sci. *322*, 103035. https://doi.org/10.1016/j.cis.2023.103035.
20. Tang, H., Gao, Y., Zhang, J., Li, Z., Gao, Q., Cai, P., Chen, X., Guo, X., van Esch, J.H., Wang, Y., and Xuan, F.Z. (2025). Harnessing the Hofmeister Effect for Dynamic Self-Assembly of Supramolecular Hydrogels. Angew. Chem. Int. Ed. *64*, e202505417. https://doi.org/10.1002/anie.202505417.
21. Wang, H., Zheng, Y.T., Zhang, J., Gao, Y., Chen, J., Cai, P., Wang, J., van Esch, J.H., Guo, X., Li, H., and Wang, Y. (2025). Synthesis of Abiotic Supramolecular Polymers Inside Living Cells via Organocatalysis-Mediated Self-Assembly. Angew. Chem. Int. Ed. *64*, e202500998. https://doi.org/10.1002/anie.202500998.
22. Ogden, W.A., and Guan, Z. (2020). Redox Chemical-Fueled Dissipative Self-Assembly of Active Materials. ChemSystemsChem *2*, e1900030. https://doi.org/10.1002/syst.201900030.
23. Kuila, S., and Nanda, J. (2024). Cysteine-Based Dynamic Self-Assembly and Their Importance in the Origins of Life. ChemSystemsChem *6*, e202400022. https://doi.org/10.1002/syst.202400022.
24. Sarkar, A., Swinkels, P.J.M., Duttenhofer, L., Besenius, P., and Walther, A. (2025). Photoactivated Enzymatic Reaction Network Enables Spatiotemporal Programming of Thiol/Disulfide Redox Systems. Angew. Chem. Int. Ed. *64*, e202503822. https://doi.org/10.1002/anie.202503822.
25. Vial, L., Ludlow, R.F., Leclaire, J., Pérez-Fernandez, R., and Otto, S. (2006). Controlling the biological effects of spermine using a synthetic receptor. J. Am. Chem. Soc. *128*, 10253–10257. https://doi.org/10.1021/ja062536b.
26. Dumartin, M., Septavaux, J., Donnier-Maréchal, M., Jeamet, E., Dumont, E., Perret, F., Vial, L., and Leclaire, J. (2020). The dark side of disulfide-based dynamic combinatorial chemistry. Chem. Sci. *11*, 8151–8156. https://doi.org/10.1039/d0sc02399j.
27. Vial, L., Perret, F., and Leclaire, J. (2022). Dyn[n]arenes: Versatile Platforms To Study the Interplay between Covalent and Noncovalent Bonds. Eur. J. Org. Chem. *2022*, e202101274. https://doi.org/10.1002/ejoc.202101274.
28. Chetot, T., Marocco Stuardi, F., Forot, A., Ducreux, M., Baudouin, A., Chefdeville, E., Perret, F., Vial, L., and Leclaire, J. (2024). Switching between Nonisoenergetic Dynamic Covalent Reactions Using Host-Guest Chemistry. J. Am. Chem. Soc. *146*, 13580–13587. https://doi.org/10.1021/jacs.4c03400.
29. Mei, J., Leung, N.L.C., Kwok, R.T.K., Lam, J.W.Y., and Tang, B.Z. (2015). Aggregation-induced emission: together we shine, united we soar. Chem. Rev. *115*, 11718–11940. https://doi.org/10.1021/acs.chemrev.5b00263.
30. Cheng, D.-B., Zhang, X.-H., Gao, Y.-J., Ji, L., Hou, D., Wang, Z., Xu, W., Qiao, Z.-Y., and Wang, H. (2019). Endogenous reactive oxygen species-triggered morphology transformation for enhanced cooperative interaction with mitochondria. J. Am. Chem. Soc. *141*, 7235–7239. https://doi.org/10.1021/jacs.8b07727.
31. Wang, Y., Nie, J., Fang, W., Yang, L., Hu, Q., Wang, Z., Sun, J.Z., and Tang, B.Z. (2020). Sugar-Based Aggregation-Induced Emission Luminogens: Design, Structures, and Applications. Chem. Rev. *120*, 4534–4577. https://doi.org/10.1021/acs.chemrev.9b00814.
32. Li, J., Wang, J., Li, H., Song, N., Wang, D., and Tang, B.Z. (2020). Supramolecular materials based on AIE luminogens (AIEgens): construction and applications. Chem. Soc. Rev. *49*, 1144–1172. https://doi.org/10.1039/c9cs00495e.
33. Guan, W.-L., Chen, J.-F., Liu, J., Shi, B., Yao, H., Zhang, Y.-M., Wei, T.-B., and Lin, Q. (2024). Macrocycles-assembled AIE supramolecular polymer networks. Coord. Chem. Rev. *507*, 215717. https://doi.org/10.1016/j.ccr.2024.215717.
34. Yang, J., Wang, X., Wu, X., Lyu, Y., Papageorgiou, A.C., and Li, J. (2025). Quantitative synthesis of dynamic combinatorial macrocycles accelerated by preorganization of AIEgens for live visualization of drug release. Cell Rep. Phys. Sci. *6*, 102355. https://doi.org/10.1016/j.xcrp.2024.102355.
35. Wang, P., Yan, X., and Huang, F. (2014). Host-guest complexation induced emission: a pillar[6]arene-based complex with intense fluorescence in dilute solution. Chem. Commun. *50*, 5017–5019. https://doi.org/10.1039/c4cc01560f.
36. Zhang, Y., Ourri, B., Skowron, P.-T., Jeamet, E., Chetot, T., Duchamp, C., Belenguer, A.M., Vanthuyne, N., Cala, O., Dumont, E., et al. (2023). Self-assembly of achiral building blocks into chiral cyclophanes using non-directional interactions. Chem. Sci. *14*, 7126–7135. https://doi.org/10.1039/D3SC01235B.
37. Mariño Pérez, L., Ielasi, F.S., Bessa, L.M., Maurin, D., Kragelj, J., Blackledge, M., Salvi, N., Bouvignies, G., Palencia, A., and Jensen, M.R. (2022). Visualizing protein breathing motions associated with aromatic ring flipping. Nature *602*, 695–700. https://doi.org/10.1038/s41586-022-04417-6.
38. Akke, M., and Weininger, U. (2023). NMR studies of aromatic ring flips to probe conformational fluctuations in proteins. J. Phys. Chem. B *127*, 591–599. https://doi.org/10.1021/acs.jpcb.2c07258.
39. Roth, P., Meyer, R., Harley, I., Landfester, K., Lieberwirth, I., Wagner, M., Ng, D.Y.W., and Weil, T. (2023). Supramolecular assembly guided by photolytic redox cycling. Nat. Synth. *2*, 980–988. https://doi.org/10.1038/s44160-023-00343-1.
40. Du, X., Zhou, J., Shi, J., and Xu, B. (2015). Supramolecular hydrogelators and hydrogels: from soft matter to molecular biomaterials. Chem. Rev. *115*, 13165–13307. https://doi.org/10.1021/acs.chemrev.5b00299.
41. Ren, Y., Zhou, Z., Maxeiner, K., Kaltbeitzel, A., Harley, I., Xing, J., Wu, Y., Wagner, M., Landfester, K., Lieberwirth, I., et al. (2024). Supramolecular Assembly in Live Cells Mapped by Real-Time Phasor-Fluorescence Lifetime Imaging. J. Am. Chem. Soc. *146*, 11991–11999. https://doi.org/10.1021/jacs.4c01279.
42. Xu, H.B., Chen, H.Y., Lv, J., Chen, B.B., Zhou, Z.R., Chang, S., Gao, Y.T., Huang, W.F., Ye, M.J., Cheng, Z.J., et al. (2023). Schiff Base Reaction in a Living Cell: In Situ Synthesis of a Hollow Covalent Organic Polymer To Regulate Biological Functions. Angew. Chem. Int. Ed. *62*, e202311002. https://doi.org/10.1002/anie.202311002.
43. Hart, P.D., and Young, M.R. (1991). Ammonium chloride, an inhibitor of phagosome-lysosome fusion in macrophages, concurrently induces phagosome-endosome fusion, and opens a novel pathway: studies of a pathogenic mycobacterium and a nonpathogenic yeast. J. Exp. Med. *174*, 881–889. https://doi.org/10.1084/jem.174.4.881.
44. Cervia, L.D., Chang, C.-C., Wang, L., and Yuan, F. (2017). Distinct effects of endosomal escape and inhibition of endosomal trafficking on gene delivery via electrotransfection. PLoS One *12*, e0171699. https://doi.org/10.1371/journal.pone.0171699.
45. Liu, Z., Guo, J., Qiao, Y., and Xu, B. (2023). Enzyme-instructed intracellular peptide assemblies. Acc. Chem. Res. *56*, 3076–3088. https://doi.org/10.1021/acs.accounts.3c00542.
46. Belosludtsev, K.N., Ilzorkina, A.I., Belosludtseva, N.V., Sharapov, V.A., Penkov, N.V., Serov, D.A., Karagyaur, M.N., Nedopekina, D.A., Davletshin, E.V., Solovieva, M.E., et al. (2022). Comparative study of cytotoxic and membranotropic properties of betulinic Acid-F16 conjugate on breast adenocarcinoma cells (MCF-7) and primary human fibroblasts. Biomedicines *10*, 2903. https://doi.org/10.3390/biomedicines10112903.